

Conditionally rigorous mitigation of multiqubit measurement errors

Michael R. Geller¹

¹*Center for Simulational Physics, University of Georgia, Athens, Georgia 30602, USA*

(Dated: September 9, 2021)

Several techniques have been recently introduced to mitigate errors in near-term quantum computers without the overhead required by quantum error correcting codes. While most of the focus has been on gate errors, measurement errors are significantly larger than gate errors on some platforms. A widely used *transition matrix error mitigation* (TMEM) technique uses measured transition probabilities between initial and final classical states to correct subsequently measured data. However from a rigorous perspective, the noisy measurement should be calibrated with perfectly prepared initial states and the presence of any state-preparation error corrupts the resulting mitigation. Here we develop a measurement error mitigation technique, conditionally rigorous TMEM, that is not sensitive to state-preparation errors and thus avoids this limitation. We demonstrate the importance of the technique for high-precision measurement and for quantum foundations experiments by measuring Mermin polynomials on IBM Q superconducting qubits. An extension of the technique allows one to correct for both state-preparation and measurement (SPAM) errors in expectation values as well; we illustrate this by giving a protocol for fully SPAM-corrected quantum process tomography.

There is a large effort focused on the development of practical applications for near-term quantum computers [1–4], for which effective error characterization [5–8] and mitigation [9–35] are essential. Also interesting is the use of near-term quantum computers for studying foundational problems in quantum mechanics and quantum information science, such verifying entanglement [33–44], finding consistent histories [45], and observing information scrambling [46–48], for which high-precision measurement is also required.

In gate-based quantum computers, where errors are separated into state-preparation errors, gate errors, and measurement errors, measurement errors are often the largest, and they can increase with register size due to persistent crosstalk [8, 30, 31]. A well-known technique for mitigating these errors is to measure the matrix T of transition probabilities between all initially prepared and observed classical states $x \in \{0,1\}^n$ on an empty (identity) circuit, and then minimize $\|Tp_{\text{corr}} - p_{\text{noisy}}\|_2^2$ subject to constraints $0 \leq p_{\text{corr}}(x) \leq 1$ and $\|p_{\text{corr}}\|_1 = 1$ to correct subsequently measured probability distributions [23–35]. Here T is a $2^n \times 2^n$ stochastic matrix with elements

$$T(x|x') = \Pr(x|x') = \text{tr}(E_x \rho_{x'}), \quad (1)$$

where $\{E_x\}_{x \in \{0,1\}^n}$ is the noisy multiqubit POVM, $\rho_{x'}$ is an initially prepared state, ideally equal to the classical state $|x'\rangle\langle x'|$, and n is the number of qubits in the processor or active register. Each column of T is the raw conditional probability distribution $\Pr(x|x')$ measured immediately after preparing x' . p_{noisy} is a given measured probability distribution expressed as a vector, and p_{corr} is the corrected distribution. $\|\cdot\|_2$ is the Euclidean norm

and $\|\cdot\|_1$ is the ℓ_1 -norm. An implementation of this *transition matrix error mitigation* (TMEM) technique is available in qiskit [49], IBM Q’s software development kit, and TMEM variations based on maximum likelihood estimation [26] and iterative Bayesian unfolding [28] have also been investigated.

Despite the wide use of TMEM, its theoretical justification has only recently been investigated [27, 50]. This work showed that imperfect measurements described by POVMs that are strictly diagonal in the classical basis—representing a type of biased classical noise—can be exactly corrected (up to statistical errors) by following the protocol described above but with a different matrix, which we write as

$$\Gamma(x|x') := \text{tr}(E_x |x'\rangle\langle x'|) = \langle x'|E_x|x'\rangle, \quad (2)$$

which has no state-preparation error. Reconstructing noisy measurement via detector tomography [51], which also assumes perfect state preparation, leads to the same conclusion. But how can we obtain Γ in the presence of inevitable state-preparation errors?

The need to prepare accurate classical states is a frequent requirement in experimental quantum computation, beyond the example (2). An extension of our technique can be used to correct other expectation values for both state-preparation and measurement (SPAM) errors. An example of independent interest, SPAM-corrected quantum process tomography, is given at the end of the paper.

In [50] we calculated Γ for individual superconducting qubits by using single-qubit gate-set tomography (GST) [52–54], which simultaneously estimated a prepared state $\rho_0 \approx |0\rangle\langle 0|$, the $\pi/2$ rotations $G_x \approx e^{-i(\pi/4)X}$

and $G_y \approx e^{-i(\pi/4)Y}$, and the 2-outcome POVM elements $E_0 \approx |0\rangle\langle 0|$ and $E_1 = I - E_0$. Here X and Y are Pauli matrices and I is the identity. The \approx symbol means that, when the errors are small, the noisy quantities are close to the indicated targets. The estimated $E_{0,1}$ were found to be nearly diagonal, consistent with the expectation that the dominant source of measurement error in transmon qubits is T_1 relaxation during dispersive readout [55, 56]. The resulting Γ matrices, obtained from the estimated POVM, were found to be significantly different than the concurrently measured T matrices. But extending this approach beyond one or two qubits is not practical due to the high sample complexity of multiqubit GST.

In this work we introduce and demonstrate a technique to estimate Γ by combining TMEM with *single-qubit* GST for each qubit in the register. Our approach assumes that the prepared classical states are separable, i.e., we neglect *entangling* crosstalk errors during state preparation (this restriction is lifted below after making additional locality assumptions). In this case knowledge of the noisy $\rho_{x'}$ on each qubit, as estimated by GST, also specifies a particular linear combination of noisy initial states that is equivalent to each *ideal* classical state $|x'\rangle\langle x'|$, up to statistical errors. Our technique combines ideas from TMEM [23–35], tomography [52–54], and quasiprobability decompositions [10, 11, 14], and can be used whenever a probability distribution is estimated.

We now show that (2) can be experimentally measured by expressing it as a linear combination of expectation values that are measured with no ideal state-preparation assumption. This is possible because GST reveals the density matrices of the noisy states (a brief introduction to GST and a discussion of its assumptions and limitations are provided in [57]). First note that any single-qubit state ρ can be written as a unique linear combination of the four ideal projectors

$$\{\pi_0, \pi_1, \pi_+, \pi_{+i}\} \quad (3)$$

where

$$\pi_0 = \begin{pmatrix} 1 & 0 \\ 0 & 0 \end{pmatrix}, \quad \pi_1 = \begin{pmatrix} 0 & 0 \\ 0 & 1 \end{pmatrix}, \quad (4)$$

$$\pi_+ = \frac{1}{2} \begin{pmatrix} 1 & 1 \\ 1 & 1 \end{pmatrix}, \quad \pi_{+i} = \frac{1}{2} \begin{pmatrix} 1 & -i \\ i & 1 \end{pmatrix}. \quad (5)$$

The expansion coefficients (quasiprobabilities) are purely real. In terms of ρ 's Bloch vector $\vec{r} = (x, y, z)$ we have

$$\rho = \left(\frac{1-x-y+z}{2}\right) \pi_0 + \left(\frac{1-x-y-z}{2}\right) \pi_1 + x \pi_+ + y \pi_{+i}. \quad (6)$$

Next we consider, for each qubit in the register, a set of four noisy initial states

$$\{\rho_0, \rho_1, \rho_+, \rho_{+i}\}, \quad (7)$$

where ρ_λ is the noisy state prepared after attempting to prepare π_λ , which we will learn from GST. For consistency with what follows, the states ρ_1 , ρ_+ , and ρ_{+i}

are to be prepared specifically by applying G_x^2 , G_y , and G_x^3 to ρ_0 , respectively, where $G_x \approx e^{-i(\pi/4)X}$ and $G_y \approx e^{-i(\pi/4)Y}$ are $\pi/2$ rotations. Then we have

$$\rho_\lambda = \sum_{\lambda' \in \{0,1,+,+i\}} L_{\lambda\lambda'} \pi_{\lambda'}, \quad \lambda \in \{0,1,+,+i\} \quad (8)$$

with the 4×4 matrix L inferred from GST by using (6). ρ_0 is directly estimated from GST, and the remaining states are calculated afterwards by acting on ρ_0 with the estimated noisy gates G_x and G_y . In tomographic notation,

$$|\rho_1\rangle\rangle = G_x^2 |\rho_0\rangle\rangle \quad (9)$$

$$|\rho_+\rangle\rangle = G_y |\rho_0\rangle\rangle \quad (10)$$

$$|\rho_{+i}\rangle\rangle = G_x^3 |\rho_0\rangle\rangle, \quad (11)$$

where $|\rho_\lambda\rangle\rangle$ and G_μ ($\mu=x,y$) are the states and gates in the Pauli basis

$$|\rho_\lambda\rangle\rangle_\sigma = \frac{\text{tr}(\rho_\lambda \sigma)}{2} \quad \text{and} \quad (G_\mu)_{\sigma\sigma'} = \frac{\text{tr}[\sigma G_\mu(\sigma')]}{2}, \quad (12)$$

where G_μ is the channel representing the noisy G_μ , and $\sigma, \sigma' \in \{I, X, Y, Z\}$.

In the error-free case L is equal to the 4×4 identity. If the state-preparation errors are not too large the noisy L can be inverted, yielding, for a single qubit

$$\pi_\lambda = \sum_{\lambda' \in \{0,1,+,+i\}} (L^{-1})_{\lambda\lambda'} \rho_{\lambda'}. \quad (13)$$

The result (13) provides a representation for the ideal single-qubit states (3) in terms of the actual noisy ones, and can be used in other expectation value measurements; we apply (13) to process tomography below.

Using (13) in (2) leads to

$$\Gamma(x|x') = \sum_{\lambda_1 \cdots \lambda_n} (L_1^{-1})_{x'_1 \lambda_1} \cdots (L_n^{-1})_{x'_n \lambda_n} \text{tr}(E_x \rho_{\lambda_1} \cdots \rho_{\lambda_n}), \quad (14)$$

where $x, x' \in \{0,1\}^n$ are classical states, x'_i is the i th bit of x' , L_i is the matrix in (8) for qubit i , and $\rho_{\lambda_1} \cdots \rho_{\lambda_n}$ is the n -qubit tensor product

$$\rho_{\lambda_1} \otimes \rho_{\lambda_1} \otimes \cdots \otimes \rho_{\lambda_n} \quad (15)$$

of the noisy basis states from (7). In condensed notation we can write (14) as

$$\Gamma(x|x') = \sum_{\lambda \in \{0,1,+,+i\}^n} (L^{-1})_{x'\lambda} \text{tr}(E_x \rho_\lambda), \quad (16)$$

where $L = L_1 \otimes L_2 \otimes \cdots \otimes L_n$. This expression provides an estimate for Γ in terms of the 4^n noisy measurements $\text{tr}(E_x \rho_\lambda)$. Although the exact Γ is necessarily stochastic, sampling errors may result in a slightly non-stochastic estimate $\hat{\Gamma}$, and in these cases we replace $\hat{\Gamma}$ by the stochastic matrix closest in Frobenius distance.

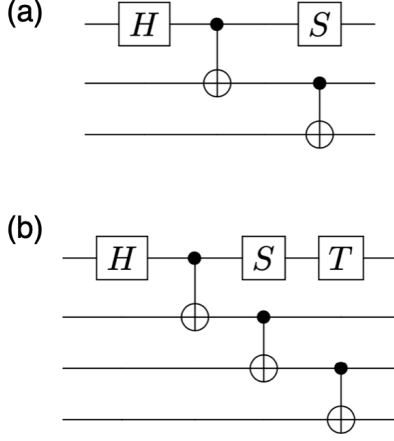


FIG. 1. Circuits to prepare (a) the three-qubit state (18) and (b) the four-qubit state (20). H , S , and T are the standard Hadamard, $\pi/2$ phase, and $\pi/4$ phase gates, respectively.

We demonstrate conditionally rigorous TMEM on the IBM Q superconducting processor `ibmq_santiago`. This 5-qubit chip with a linear chain geometry was added in 2020 and features a quantum volume of 32, the highest currently available on the IBM Q network. Gate errors, estimated by randomized benchmarking and provided by the backend, are summarized in [57]. We ran single-qubit GST and calculated the L matrices for qubits $\{Q_0, Q_1, Q_2, Q_3\}$ using our BQP data acquisition software combined with pyGSTi [58]. We measured 589 distinct circuits up to length 16 (18 including fiducials) on each qubit, and generated robust CPTP estimates for the state ρ_0 , the $\pi/2$ rotations G_x and G_y , and the two-outcome POVM. All circuits were measured with 8k measurement samples. The detailed GST results and L matrices are provided in [57]. Conditionally rigorous TMEM can be independently validated in the $n=1$ limit by comparing the single-qubit Γ matrix obtained from quasiprobability decompositions, via (16), with that computed directly from the GST-estimated POVM [50]. The results of this check confirm the accuracy of (16) in the $n=1$ case and are also provided in [57]. A classical simulation also validates the technique on a simplified error model consistent with the `ibmq_santiago` [57].

Next we measure and correct Mermin polynomials [59]. As multipartite generalizations of Bell's inequality, the Mermin inequalities have foundational interest for potentially violating local realism if specific combinations of Pauli expectation values are sufficiently large. Although the presence of detection and locality loopholes prevent us from rejecting local realism without additional assumptions, the accuracy and rigorous justification of any error mitigation technique is clearly important for this experimental test. This example is also interesting because there is a rich history of measuring Mermin

polynomials with photons [60], superconducting qubits [34, 36–40] and ions [42], enabling comparisons across platforms and over time. Of course any expectation value (or any quantity derived from experimentally estimated probability distributions) can be similarly corrected. We measure the three-qubit Mermin polynomial

$$M_3 = \langle XXY \rangle + \langle XYX \rangle + \langle YXX \rangle - \langle YYY \rangle \quad (17)$$

on the state

$$\frac{|000\rangle + i|111\rangle}{\sqrt{2}}, \quad (18)$$

and the four-qubit polynomial

$$\begin{aligned} M_4 = & \langle XXXY \rangle + \langle XXYX \rangle + \langle XYXX \rangle + \langle YXXX \rangle \\ & + \langle XXY Y \rangle + \langle XYXY \rangle + \langle XYYX \rangle + \langle YXXY \rangle \\ & + \langle YXYX \rangle + \langle YYXX \rangle - \langle XXXX \rangle - \langle XYYY \rangle \\ & - \langle YXYY \rangle - \langle YYXY \rangle - \langle YYYX \rangle - \langle YYYY \rangle \end{aligned} \quad (19)$$

on the state

$$\frac{|0000\rangle + e^{3\pi i/4}|1111\rangle}{\sqrt{2}}. \quad (20)$$

The states (18) and (20) are chosen because they allow for a maximal violation of local realism in the ideal limit. They are prepared by the circuits shown in Fig. 1. Measurement of X and Y are obtained by applying H and HS^\dagger prior to a Z basis measurement. We measure every Pauli expectation value in (17) and (19) and do not assume that the noisy states have the symmetries under qubit exchange possessed by their ideal targets.

TABLE I. Mermin polynomials (17) and (19) measured on the IBM Q device `ibmq_santiago` with 8k measurement samples. LR is the maximum value consistent with local realism. QM is the maximum value allowed by quantum mechanics. Experimental data are reported as the average over $N=16$ independent estimations plus/minus the standard error σ/\sqrt{N} , where σ^2 is the variance of the N samples. The T and Γ columns give the polynomial values after correcting the raw probability distributions with the T and Γ matrices.

	LR	QM	Raw data	T matrix	Γ matrix
M_3	2	4	3.618 ± 0.004	3.998 ± 0.002	3.814 ± 0.004
M_4	4	$8\sqrt{2}$	8.797 ± 0.212	10.232 ± 0.247	9.037 ± 0.218

The experimental results are summarized in Table I. Polynomial M_3 was measured on qubits $\{Q_0, Q_1, Q_2\}$ after preparing (18), whereas M_4 was measured on qubits $\{Q_0, Q_1, Q_2, Q_3\}$ after preparing (20). We find that in both cases the effects of measurement errors are significant, as reflected in the differences between the raw and rigorously corrected values. We also find that the T matrix *overestimates* the entanglement, which means it should not be trusted in quantum foundations experiments such as this one. The T matrix result for M_3 is unphysical as it nearly saturates the quantum upper bound,

yet also includes two CNOT gate errors of magnitude 0.008 and 0.007 [57]. The differences between correction by T and Γ is statistically significant for both polynomials. The complete data set and comparison with previous experiments on superconducting qubits is provided in [57].

TABLE II. Classically simulated measurement and mitigation of the 4-qubit Mermin polynomial. Simulation results are reported as the average over $N=16$ random POVM samples.

	LR	QM	Exact($\eta=0.2$)	Raw data	T matrix	Γ matrix
M_4	4	$8\sqrt{2}$	9.051	8.962	9.821	9.067

To test the accuracy of rigorous TMEM, we summarize in Table II the results of a purely classical simulation of conditionally rigorous M_4 mitigation, assuming a simplified error model designed to be similar to ibmq.santiago [57]. Here η is the error strength of a depolarization channel applied to (20) to account for imperfect GHZ state preparation. In the simulation, the multi-qubit POVM consists of diagonal but otherwise random positive semidefinite matrices. Importantly, the measurement operators are *not* separable; they contain correlated multiqubit measurement errors. As the measurement-error-free value of M_4 is known in this simulation (the “Exact” column in Table II), the accuracy of conditionally rigorous TMEM can be tested. We find that GST successfully learns the simplified error model and that the Γ matrix correctly mitigates the correlated measurement errors [57]. However we note that rigorous TMEM can fail if GST does (see [57] for additional discussion).

In the entanglement estimation above, TMEM is used to remove measurement errors from the Mermin polynomials. We accept the entangled states actually produced in the noisy device, and estimate their entanglement using Γ -based TMEM, but we do not (and should not) attempt to correct for the imperfect entangled state preparation. However conditionally rigorous TMEM can be extended to the estimation of expectation values with both initial states and measurements corrected: Here we give an application to fully SPAM-corrected quantum process tomography (QPT). Specifically, we consider the estimation of the Pauli transfer matrix (12) for an arbitrary CPTP channel $\rho \mapsto \rho' = \Phi(\rho)$, defined as

$$\Phi_{\sigma\sigma'} := \frac{\text{tr}[\sigma \Phi(\sigma')]}{d}. \quad (21)$$

Here $\sigma, \sigma' \in \{I, X, Y, Z\}^n$ and $d = 2^n$ is the Hilbert space dimension. The measurement of observable σ is obtained following the standard method of applying gates after the channel to transform to the diagonal basis, which is then calculated from a measured n -qubit probability distribution $\text{Pr}(x)$. The probability distribution can be corrected for measurement error using the Γ matrix (2), as explained above. Next, we use (13) to simulate the ideal

preparation of σ' . For a single qubit i , we obtain

$$\begin{aligned} \begin{pmatrix} I \\ X \\ Y \\ Z \end{pmatrix} &= \begin{pmatrix} 1 & 1 & 0 & 0 \\ -1 & -1 & 2 & 0 \\ -1 & -1 & 0 & 2 \\ 1 & -1 & 0 & 0 \end{pmatrix} \begin{pmatrix} \pi_0 \\ \pi_1 \\ \pi_+ \\ \pi_{+i} \end{pmatrix} = M \begin{pmatrix} \pi_0 \\ \pi_1 \\ \pi_+ \\ \pi_{+i} \end{pmatrix} \\ &= M L_i^{-1} \begin{pmatrix} \rho_0 \\ \rho_1 \\ \rho_+ \\ \rho_{+i} \end{pmatrix}, \end{aligned} \quad (22)$$

relating ideal Pauli’s to noisy initial states (7). Then similarly to (16), $\Phi_{\sigma\sigma'}$ is constructed from the measured values of $\text{tr}[\sigma \Phi(\rho_\lambda)]$ for all $\sigma \in \{I, X, Y, Z\}^n$ and $\lambda \in \{0, 1, +, +i\}^n$.

In conclusion, we have considered transition matrix error mitigation [23–35] based on the matrix (1). By instead using the matrix Γ defined in (2), we can correct measurement errors without contamination by state-preparation errors. We show how to obtain Γ by performing single-qubit GST on each qubit of the register, plus 4^n additional measurements. This is an increase in sample complexity over the 2^n measurements required for a complete estimation of T , but the resulting error mitigation is rigorously exact, conditioned on the following assumptions:

1. The noisy classical states are separable.
2. The multiqubit POVM is diagonal in the classical basis. However the measurement operators are not assumed to be separable.
3. GST converges to a gateset that accurately models the input data, and the gauge choice accurately separates state preparation, gate, and measurement errors.

Note that we don’t assume that the G_x and G_y gates are truly single-qubit. Any entanglement with neighbors is seen by GST as another decoherence mechanism, which it will try to learn (see [57] for further discussion).

Condition 1 means that we can learn the explicit form of the noisy initial states through single-qubit GST. However conditionally rigorous TMEM can be generalized to allow for entangled inputs, assuming they have local support: If a constant number m qubits are entangled, then these entangled states can also be learned with m -qubit GST. Condition 2 is a sufficient condition for the possibility of rigorous correction [27, 50]. Condition 3 means that the violation of the learned model by the data is negligible. GST may fail to converge if the noise is nonstationary or strongly non-Markovian. Condition 3 also reflects the impossibility for any tomographic technique to uniquely decompose observed nonidealities into separate state, gate, and POVM errors [52, 61]. GST chooses a gauge to maximize the overall fit of the model to the ideal

targets, and we are implicitly assuming that the resulting decomposition is reliable (our classical simulation [57] supports this). Conditioned on these assumptions, rigorous TMEM should help make high-precision and foundational quantum information science experiments possible with gate-based quantum computing platforms.

Acknowledgments. I am grateful to IBM Research for making their superconducting processors available to the quantum computing community. This work does not reflect the views or opinions of IBM or any of their employees. I would also like to thank the anonymous referees for suggestions that improved the presentation of this paper.

-
- [1] A. W. Harrow and A. Montanaro, *Nature* **549**, 203 (2017).
 - [2] J. Preskill, *Quantum* **2**, 79 (2018).
 - [3] S. Bravyi, D. Gosset, R. König, and M. Tomamichel, *Nat. Phys.* (2020), <https://doi.org/10.1038/s41567-020-0948-z>.
 - [4] F. Arute, K. Arya, R. Babbush, D. Bacon, J. C. Bardin, R. Barends, R. Biswas, S. Boixo, F. G. S. L. Brandao, D. A. Buell, B. Burkett, Y. Chen, Z. Chen, B. Chiaro, R. Collins, W. Courtney, A. Dunsworth, E. Farhi, B. Foxen, A. Fowler, C. Gidney, M. Giustina, R. Graff, K. Guerin, S. Habegger, M. P. Harrigan, M. J. Hartmann, A. Ho, M. Hoffmann, T. Huang, T. S. Humble, S. V. Isakov, E. Jeffrey, Z. Jiang, D. Kafri, K. Kechedzhi, J. Kelly, P. V. Klimov, S. Knysh, A. Korotkov, F. Kostritsa, D. Landhuis, M. Lindmark, E. Lucero, D. Lyakh, S. Mandrà, J. R. McClean, M. McEwen, A. Megrant, X. Mi, K. Michielsen, M. Mohseni, J. Mutus, O. Naaman, M. Neeley, C. Neill, M. Y. Niu, E. Ostby, A. Petukhov, J. C. Platt, C. Quintana, E. G. Rieffel, P. Roushan, N. C. Rubin, D. Sank, K. J. Satzinger, V. Smelyanskiy, K. J. Sung, M. D. Trevithick, A. Vainsencher, B. Villalonga, T. White, Z. J. Yao, P. Yeh, A. Zalcman, H. Neven, and J. M. Martinis, *Nature (London)* **574**, 505 (2019).
 - [5] A. Erhard, J. J. Wallman, L. Postler, M. Meth, R. Stricker, E. A. Martinez, P. Schindler, T. Monz, J. Emerson, and R. Blatt, *Nat. Commun.* **10**, 5347 (2019).
 - [6] S. T. Flammia and J. J. Wallman, “Efficient estimation of Pauli channels,” arXiv: 1907.12976.
 - [7] R. Harper, S. T. Flammia, and J. J. Wallman, *Nat. Phys.* (2020), <https://doi.org/10.1038/s41567-020-0992-8>.
 - [8] K. E. Hamilton, T. Kharazi, T. Morris, A. J. McCaskey, R. S. Bennink, and R. C. Pooser, “Scalable quantum processor noise characterization,” arXiv: 2006.01805.
 - [9] Y. Li and S. C. Benjamin, *Phys. Rev. X* **7**, 021050 (2017).
 - [10] K. Temme, S. Bravyi, and J. M. Gambetta, *Phys. Rev. Lett.* **119**, 180509 (2017).
 - [11] S. Endo, S. C. Benjamin, and Y. Li, *Phys. Rev. X* **8**, 031027 (2018).
 - [12] E. F. Dumitrescu, A. J. McCaskey, G. Hagen, G. R. Jansen, T. D. Morris, T. Papenbrock, R. C. Pooser, D. J. Dean, and P. Lougovski, *Phys. Rev. Lett.* **120**, 210501 (2017).
 - [13] A. Kandala, K. Temme, A. D. Córcoles, A. Mezzacapo, J. M. Chow, and J. M. Gambetta, *Nature* **567**, 491 (2019).
 - [14] C. Song, J. Cui, H. Wang, J. J. Hao, H. Feng, and Y. Li, *Sci. Adv.* **5**, eaaw5686 (2019).
 - [15] S. S. Tannu and M. K. Qureshi, in *The 52nd Annual IEEE/ACM International Symposium on Microarchitecture* (2019) “Mitigating measurement errors in quantum computers by exploiting state-dependent bias”.
 - [16] S. S. Tannu and M. K. Qureshi, in *The 52nd Annual IEEE/ACM International Symposium on Microarchitecture* (2019) “Ensemble of diverse mappings: Improving reliability of quantum computers by orchestrating dissimilar mistakes”.
 - [17] M. Otten and S. K. Gray, *Phys. Rev. A* **99**, 012338 (2019).
 - [18] H. Kwon and J. Bae, “A hybrid quantum-classical approach to mitigating measurement errors,” arXiv: 2003.12314.
 - [19] P. Czarnik, A. Arrasmith, P. J. Coles, and L. Cincio, “Error mitigation with Clifford quantum-circuit data,” arXiv: 2005.10189.
 - [20] L. Funcke, T. Hartung, K. Jansen, S. Kühn, P. Stornati, and X. Wang, “Measurement error mitigation in quantum computers through classical bit-flip correction,” arXiv: 2007.03663.
 - [21] R. Hicks, C. W. Bauer, and B. Nachman, “Readout rebalancing for near term quantum computers,” arXiv: 2010.07496.
 - [22] M. Zheng, A. Li, T. Terlaky, and X. Yang, “A Bayesian approach for characterizing and mitigating gate and measurement errors,” arXiv: 2010.09188.
 - [23] A. Dewes, F. R. Ong, V. Schmitt, R. Lauro, N. Boulant, P. Bertet, D. Vion, and D. Esteve, *Phys. Rev. Lett.* **108**, 057002 (2012).
 - [24] S. Debnath, N. M. Linke, C. Figgatt, K. A. Landsman, K. Wright, and C. Monroe, *Nature* **536**, 63 (2016).
 - [25] V. Havlíček, A. D. Córcoles, K. Temme, A. W. Harrow, A. Kandala, J. M. Chow, and J. M. Gambetta, *Nature* **567**, 209 (2019).
 - [26] Y. Chen, M. Farahzad, S. Yoo, and T.-C. Wei, *Phys. Rev. A* **100**, 052315 (2019), arXiv: 1904.11935.
 - [27] F. B. Maciejewski, Z. Zimborás, and M. Oszmaniec, *Quantum* **4**, 257 (2020), arXiv: 1907.08518.
 - [28] B. Nachman, M. Urbanek, W. A. de Jong, and C. W. Bauer, “Unfolding quantum computer readout noise,” arXiv: 1910.01969.
 - [29] K. E. Hamilton and R. C. Pooser, “Error-mitigated data-driven circuit learning on noisy quantum hardware,” arXiv: 1911.13289.
 - [30] M. R. Geller and M. Sun, *Quantum Sci. Technol.* **6**, 025009 (2021), arXiv: 181010523.
 - [31] S. Bravyi, S. Sheldon, A. Kandala, D. C. McKay, and J. M. Gambetta, “Mitigating measurement errors in multi-qubit experiments,” arXiv: 2006.14044.
 - [32] G. S. Barron and C. J. Wood, “Measurement error mitigation for variational quantum algorithms,” arXiv: 2010.08520.
 - [33] R. C. Bialczak, M. Ansmann, M. Hofheinz, E. Lucero, M. Neeley, A. D. O’Connell, D. Sank, H. Wang, J. Wenner, M. Steffen, A. N. Cleland, and J. M. Martinis, *Nat. Phys.* **6**, 409 (2010).
 - [34] M. Neeley, R. C. Bialczak, M. Lenander, E. Lucero, M. Mariantoni, A. D. O’Connell, D. Sank, H. Wang, M. Weides, J. Wenner, Y. Yin, T. Yamamoto, A. N. Cle-

- land, and J. M. Martinis, *Nature* **467**, 570 (2010).
- [35] M. Gong, M.-C. Chen, Y. Zheng, S. Wang, C. Zha, H. Deng, Z. Yan, H. Rong, Y. Wu, S. Li, F. Chen, Y. Zhao, F. Liang, J. Lin, Y. Xu, C. Guo, L. Sun, A. D. Castellano, H. Wang, C. Peng, C.-Y. Lu, X. Zhu, and J.-W. Pan, *Phys. Rev. Lett.* **122**, 110501 (2019).
 - [36] L. DiCarlo, M. D. Reed, L. Sun, B. R. Johnson, J. M. Chow, J. M. Gambetta, L. Frunzio, S. M. Girvin, M. H. Devoret, and R. J. Schoelkopf, *Nature (London)* **467**, 574 (2010).
 - [37] D. Alsina and J. I. Latorre, *Phys. Rev. A* **94**, 012314 (2016).
 - [38] D. García-Martín and G. Sierra, *J. Appl. Math. Phys.* **6**, 1460 (2018).
 - [39] D. González, D. Fernández de la Pradilla, and G. González, “Revisiting the experimental test of Mermin’s inequalities at IBMQ,” arXiv: 2005.11271.
 - [40] W.-J. Huang, W.-C. Chien, C.-H. Cho, C.-C. Huang, T.-W. Huang, and C.-R. Chang, “Mermin’s inequalities of multiple qubits with orthogonal measurements on IBM Q 53-qubit system,” arXiv: 2005.12504.
 - [41] T. Monz, P. Schindler, J. T. Barreiro, M. Chwalla, D. Nigg, W. A. Coish, M. Harlander, W. Hänsel, M. Hennrich, and R. Blatt, *Phys. Rev. Lett.* **106**, 130506 (2011).
 - [42] B. P. Lanyon, M. Zwerger, P. Jurcevic, C. Hempel, W. Dür, H. J. Briegel, R. Blatt, and C. F. Roos, *Phys. Rev. Lett.* **112**, 100403 (2014).
 - [43] C. Song, K. Xu, H. Li, Y.-R. Zhang, X. Zhang, W. Liu, Q. Guo, Z. Wang, W. Ren, J. Hao, H. Feng, H. Fan, D. Zheng, D.-W. Wang, H. Wang, and S.-Y. Zhu, *Science* **365**, 574 (2019).
 - [44] K. X. Wei, I. Lauer, S. Srinivasan, N. Sundaresan, D. T. McClure, D. Toyli, D. C. McKay, J. M. Gambetta, and S. Sheldon, *Phys. Rev. A* **101**, 032343 (2020).
 - [45] A. Arrasmith, L. Cincio, A. T. Sornborger, W. H. Zurek, and P. J. Coles, *Nat. Commun.* **10**, 3438 (2019).
 - [46] J. Li, R. Fan, H. Wang, B. Ye, B. Zeng, H. Zhai, X. Peng, and J. Du, *Physical Review X* **7**, 031011 (2017).
 - [47] K. A. Landsman, C. Figgatt, T. Schuster, N. M. Linke, B. Yoshida, N. Y. Yao, and C. Monroe, *Nature* **567**, 61 (2019).
 - [48] M. S. Blok, V. V. Ramasesh, T. Schuster, K. O’Brien, J. M. Kreikebaum, D. Dahlen, A. Morvan, B. Yoshida, N. Y. Yao, and I. Siddiqi, *Phys. Rev. X* **11**, 021010 (2021).
 - [49] H. Abraham *et al.*, “Qiskit: An Open source Framework for Quantum Computing,” (2019).
 - [50] M. R. Geller, *Quantum Sci. Technol.* **5**, 03LT01 (2020), arXiv:2002.01471.
 - [51] A. Luis and L. L. Sánchez-Soto, *Phys. Rev. Lett.* **83**, 3573 (1999).
 - [52] R. Blume-Kohout, J. K. Gamble, E. Nielsen, J. Mizrahi, J. D. Sterk, and P. Maunz, “Robust, self-consistent, closed-form tomography of quantum logic gates on a trapped ion qubit,” arXiv: 1310.4492.
 - [53] S. T. Merkel, J. M. Gambetta, J. A. Smolin, S. Poletto, A. D. Córcoles, B. R. Johnson, C. A. Ryan, and M. Steffen, *Phys. Rev. A* **87**, 062119 (2013).
 - [54] R. Blume-Kohout, J. K. Gamble, E. Nielsen, J. Mizrahi, J. D. Sterk, and P. Maunz, *Nat. Commun.* **8**, 14485 (2017).
 - [55] F. Mallet, F. R. Ong, A. Palacios-Laloy, F. Nguyen, P. Bertet, D. Vion, and D. Esteve, *Nat. Phys.* **5**, 791 (2009).
 - [56] J. Heinsoo, C. K. Andersen, A. Remm, S. Krinner, T. Walter, Y. Salathé, S. Gasparinetti, J.-C. Besse, A. Potočník, A. Wallraff, and C. Eichler, *Phys. Rev. Applied* **10** (2018).
 - [57] See Supplemental Material at <http://link.aps.org/supplemental> for additional data and analysis.
 - [58] E. Nielsen, K. Rudinger, J. K. Gamble, and R. Blume-Kohout, “pyGSTi: A python implementation of gate set tomography,” <https://github.com/pyGSTio/pyGSTi>.
 - [59] N. D. Mermin, *Phys. Rev. Lett.* **65**, 1838 (1990).
 - [60] J.-W. Pan, D. Bouwmeester, M. Daniell, H. Weinfurter, and A. Zeilinger, *Nature* **403**, 515 (2000).
 - [61] J. Lin, B. Buonacorsi, R. Laflamme, and J. J. Wallman, *New J. Phys.* **21**, 023006 (2019).

Supplementary Information for “Conditionally rigorous mitigation of multiqubit measurement errors”

This document provides additional details about the validation and experimental implementation of the rigorous transition matrix error mitigation (TMEM) technique. In Sec. 1 we describe the IBM Q online superconducting qubits used in the experiment and give calibration results (gate errors, coherence times, and single-qubit measurement errors) provided by the backend. In Sec. 2 we provide a brief introduction to GST and discuss its limitations. In Sec. 3 we give the detailed GST results.

In Sec. 4 we provide the L matrices used in the Mermin polynomial correction. In Sec. 5 we validate the technique used to calculate the Γ matrices in the $n = 1$ case by direct comparison with single-qubit GST. In Sec. 6 we give the detailed Mermin polynomial measurement results and compare these with previous work. In Sec. 7 we present the results of an end-to-end simulation of the correction of the Mermin polynomial M_4 , further validating the rigorous TMEM technique.

1. QUBITS

In this section we discuss the online superconducting qubits used in this work. Data was taken on the IBM Q processor `ibmq_santiago` using the BQP software package developed by the author. BQP is a Python package developed to design, run, and analyze complex quantum computing and quantum information experiments using commercial backends. We demonstrate the rigorous TMEM technique using the qubits shown in Fig. S1. Calibration data supplied by the backend is summarized in Table I. Here $T_{1,2}$ are the standard Markovian decoherence times, and

$$\epsilon = \frac{T(0|1) + T(1|0)}{2} \quad (\text{S1})$$

is the single-qubit state-preparation and measurement (SPAM) error, averaged over initial classical states. The U_2 error column gives the single-qubit gate error measured by randomized benchmarking. The CNOT errors are also measured by randomized benchmarking.

TABLE I. Calibration data provided by IBM Q for the `ibmq_santiago` chip during the period of data acquisition.

Qubit	T_1 (μs)	T_2 (μs)	SPAM error ϵ	U_2 error
Q_0	108.6	151.1	0.0139	2.98e-4
Q_1	122.8	85.9	0.0137	1.73e-4
Q_2	120.1	92.4	0.0178	1.63e-4
Q_3	157.7	90.3	0.0135	1.90e-4
CNOT gates			CNOT error	
CNOT _{0,1}		CNOT _{1,0}	8.14e-3	
CNOT _{1,2}		CNOT _{2,1}	7.03e-3	
CNOT _{2,3}		CNOT _{3,2}	6.36e-3	

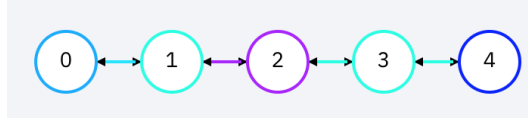


FIG. S1. Layout of IBM Q device ibmq_santiago. In this work we use qubits Q_0 , Q_1 , Q_2 and Q_3 .

2. GST PRIMER

Gate set tomography (GST) is a tomographic technique used to simultaneously estimate one or more initial states $\{\rho_i\}$, an informationally complete set of gates $\{\Phi_i\}$, modeled here as CPTP superoperators $\rho \mapsto \rho' = \Phi(\rho)$, and a POVM $\{E_x\}_{x \in \{0,1\}^n}$, all defined on a fixed register of n qubits [52–54, 58]. It works by measuring a large batch of circuits, designed to amplify errors by repeating carefully chosen germ sequences. After an iterative global optimization procedure the entire dataset is then fit to a global gateset model

$$\{\{\rho_i\}, \{\Phi_i\}, \{E_x\}\}. \quad (\text{S2})$$

GST returns a representation of this gateset along with several fidelity measures and statistical confidence bounds.

For the purposes of conditionally rigorous TMEM, it is only necessary to estimate one initial state ρ_0 and two gates per qubit, namely $\pi/2$ rotations about x and y , which we write a G_x and G_y . On each qubit we measured 589 distinct circuits up to length 16 (18 including fiducials), and used the robust CPTP estimates from pyGSTi [58]. GST also produces a single-qubit POVM for each qubit, which we do not use here.

Like any tomographic technique, GST has limitations and can fail to produce an accurate estimate. There are two principle failure modes: First the gateset may fail to converge. The reason for this is that the data is fit to a *stationary* gateset, whereas real data contain non-Markovian noise and drift. GST provides global measures of the fit of data to the estimated model (see Fig. S2 below). In our experiment we obtained a “good” fit to the estimated gateset. The second failure mode concerns the issue of tomography gauge. It is not possible for GST to produce a unique gateset; in particular, to uniquely separate a circuit error into state-preparation error, gate error, and POVM error. The most common approach, also followed here, is to choose this gauge to minimize the difference between the estimated gateset and the ideal one.

We do not have to assume that G_x and G_y are truly single-qubit gates. Any entanglement with neighboring qubits is seen by GST as another decoherence mechanism, which it will learn as long as the associated noise is stationary.

To test the accuracy of GST in our experiment, we implemented a complete end-to-end simulation of the entire procedure. This is discussed below in Sec. 7. We find that GST is able to accurately learn a planted error model using the standard gauge choice. However we note that this gauge might not apply to a highly asymmetric error model, where, for example, some elements of the model have much larger errors than others.

3. GST RESULTS

Here we give the detailed GST results provided by pyGSTi [58] for the $n = 4$ case. Tables II and III give the estimated single-qubit models and error measures, and Fig. S2 shows the model violation (caused by non-stationary noise, including drift) versus gate sequence length.

TABLE II. Reconstructed ρ_0 state and two-outcome POVM estimated by GST for the IBM Q device ibmq_santiago.

Qubit	ρ_0	G_x	G_y	E_0
Q_0	$\begin{pmatrix} 0.9849 & 0.0539 \\ 0.0539 & 0.0151 \end{pmatrix}$	$\begin{pmatrix} 1 & 0 & 0 & 0 \\ 0.0001 & 0.9999 & -0.0002 & -0.0001 \\ 0 & -0.0001 & -0.0001 & -1 \\ 0 & 0.0001 & 0.9999 & -0.0001 \end{pmatrix}$	$\begin{pmatrix} 1 & 0 & 0 & 0 \\ 0 & 0.0002 & -0.0001 & 1 \\ 0 & -0.0001 & 1 & 0.0002 \\ 0 & -1 & -0.0002 & 0.0002 \end{pmatrix}$	$\begin{pmatrix} 0.9994 & -0.0005 \\ -0.0005 & 0.0080 \end{pmatrix}$
Q_1	$\begin{pmatrix} 0.9848 & 0.0534 \\ 0.0534 & 0.0152 \end{pmatrix}$	$\begin{pmatrix} 1 & 0 & 0 & 0 \\ 0 & 1 & 0 & 0 \\ 0 & 0 & 0 & -1 \\ 0 & 0 & 1 & 0 \end{pmatrix}$	$\begin{pmatrix} 1 & 0 & 0 & 0 \\ 0 & -0.0002 & 0 & 1 \\ 0 & 0 & 1 & 0 \\ 0 & -1 & 0 & -0.0002 \end{pmatrix}$	$\begin{pmatrix} 0.9993 & 0 \\ 0 & 0.0082 \end{pmatrix}$
Q_2	$\begin{pmatrix} 0.9845 & 0.0537 \\ 0.0537 & 0.0155 \end{pmatrix}$	$\begin{pmatrix} 1 & 0 & 0 & 0 \\ 0 & 1 & 0 & 0 \\ 0 & 0 & -0.0001 & -1 \\ 0 & 0 & 1 & -0.0001 \end{pmatrix}$	$\begin{pmatrix} 1 & 0 & 0 & 0 \\ 0 & -0.0001 & 0 & 1 \\ 0 & 0 & 1 & 0 \\ 0 & -1 & 0 & -0.0001 \end{pmatrix}$	$\begin{pmatrix} 0.9995 & -0.0010 \\ -0.0010 & 0.0086 \end{pmatrix}$
Q_3	$\begin{pmatrix} 0.9846 & 0.0540 \\ 0.0540 & 0.0154 \end{pmatrix}$	$\begin{pmatrix} 1 & 0 & 0 & 0 \\ -0.0001 & 0.9997 & 0.0001 & 0.0003 \\ 0 & -0.0002 & -0.0003 & -0.9997 \\ 0.0001 & 0 & 0.9995 & -0.0002 \end{pmatrix}$	$\begin{pmatrix} 1 & 0 & 0 & 0 \\ 0.0001 & -0.0002 & 0.0001 & 0.9997 \\ 0 & -0.0001 & 0.9997 & 0 \\ 0 & -0.9998 & 0.0002 & 0 \end{pmatrix}$	$\begin{pmatrix} 1 & -0.0009 \\ -0.0009 & 0.0105 \end{pmatrix}$

TABLE III. Gate error measures.

Qubit	Gate	Entanglement infidelity	Trace distance/2	Eigenvalue entanglement infidelity
Q_0	G_x	6.31e-5	1.47e-4	6.31e-5
	G_y	1.46e-5	1.34e-4	1.46e-5
Q_1	G_x	3.84e-10	1.95e-5	5.88e-15
	G_y	1.14e-8	1.07e-4	2.09e-14
Q_2	G_x	1.08e-9	3.28e-5	4.21e-15
	G_y	4.98e-9	7.06e-5	2.22e-16
Q_3	G_x	2.74e-4	3.23e-4	2.74e-4
	G_y	2.00e-4	2.20e-4	2.00e-4

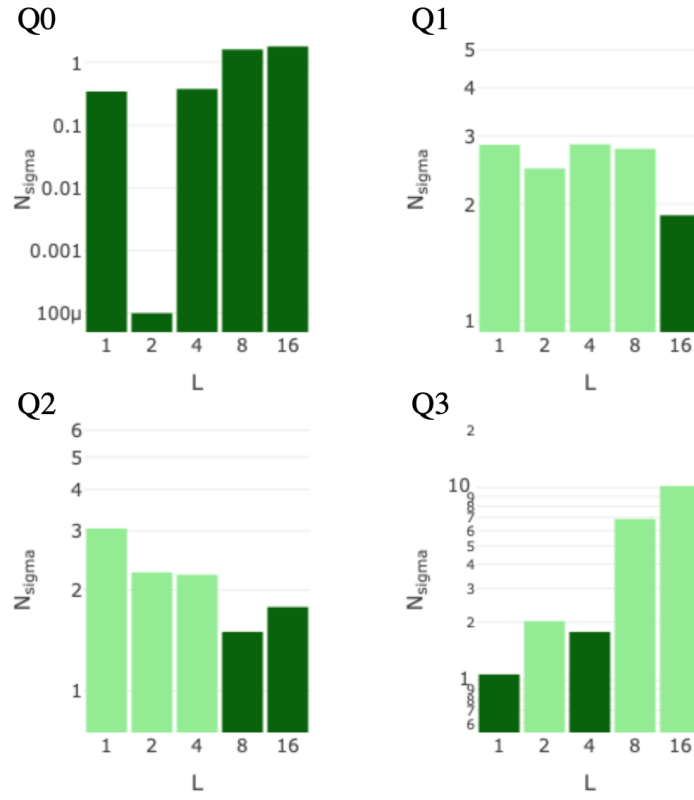


FIG. S2. GST model violation versus sequence length L .

4. L MATRICES

In Table IV we provide the calculated L matrices for the qubits used in the experiments for the $n=4$ case.

TABLE IV. L matrices.

Qubit	L
Q_0	$\begin{pmatrix} 0.9164 & -0.0535 & 0.1079 & 0.0292 \\ -0.0243 & 0.9454 & 0.1080 & -0.0291 \\ -0.0535 & 0.0543 & 0.9699 & 0.0293 \\ -0.0534 & -0.0244 & 0.1082 & 0.9697 \end{pmatrix}$
Q_1	$\begin{pmatrix} 0.9170 & -0.0527 & 0.1067 & 0.0289 \\ -0.0238 & 0.9459 & 0.1067 & -0.0288 \\ -0.0527 & 0.0542 & 0.9696 & 0.0289 \\ -0.0526 & -0.0238 & 0.1067 & 0.9697 \end{pmatrix}$
Q_2	$\begin{pmatrix} 0.9157 & -0.0533 & 0.1074 & 0.0302 \\ -0.0231 & 0.9458 & 0.1074 & -0.0301 \\ -0.0533 & 0.0542 & 0.9689 & 0.0302 \\ -0.0532 & -0.0231 & 0.1073 & 0.9689 \end{pmatrix}$
Q_3	$\begin{pmatrix} 0.9153 & -0.0538 & 0.1081 & 0.0304 \\ -0.0232 & 0.9451 & 0.1081 & -0.0301 \\ -0.0537 & 0.0544 & 0.9690 & 0.0304 \\ -0.0527 & -0.0230 & 0.1077 & 0.9680 \end{pmatrix}$

5. Γ VALIDATION

Here we validate the Γ estimation technique, based on quasiprobability decomposition, for the special case of a 1-qubit register, by comparing it with that obtained from the POVM directly estimated by single-qubit GST [50], which we denote by Γ_{POVM} . The results are shown in Table V. The concurrently measured single-qubit T matrices are also given, as are the Frobenius distances $\|\Gamma - T\|_{\text{F}}$ and $\|\Gamma - \Gamma_{\text{POVM}}\|_{\text{F}}$.

TABLE V. Γ versus Γ_{POVM} for the case $n=1$.

Qubit	Γ	Γ_{POVM}	T	$\ \Gamma - T\ _{\text{F}}$	$\ \Gamma - \Gamma_{\text{POVM}}\ _{\text{F}}$
Q_0	$\begin{pmatrix} 0.9981 & 0.0063 \\ 0.0019 & 0.9937 \end{pmatrix}$	$\begin{pmatrix} 0.9994 & 0.0080 \\ 0.0006 & 0.9920 \end{pmatrix}$	$\begin{pmatrix} 0.9838 & 0.0257 \\ 0.0163 & 0.9742 \end{pmatrix}$	3.42e-2	3.11e-3
Q_1	$\begin{pmatrix} 0.9992 & 0.0060 \\ 0.0008 & 0.9940 \end{pmatrix}$	$\begin{pmatrix} 0.9993 & 0.0082 \\ 0.0007 & 0.9918 \end{pmatrix}$	$\begin{pmatrix} 0.9845 & 0.0243 \\ 0.0155 & 0.9758 \end{pmatrix}$	3.32e-2	3.18e-3
Q_2	$\begin{pmatrix} 0.9977 & 0.0108 \\ 0.0023 & 0.9892 \end{pmatrix}$	$\begin{pmatrix} 0.9995 & 0.0086 \\ 0.0005 & 0.9914 \end{pmatrix}$	$\begin{pmatrix} 0.9819 & 0.0294 \\ 0.0181 & 0.9706 \end{pmatrix}$	3.45e-2	3.99e-3
Q_3	$\begin{pmatrix} 0.9986 & 0.0125 \\ 0.0014 & 0.9875 \end{pmatrix}$	$\begin{pmatrix} 1.0000 & 0.0105 \\ 0.0000 & 0.9895 \end{pmatrix}$	$\begin{pmatrix} 0.9829 & 0.0253 \\ 0.0171 & 0.9748 \end{pmatrix}$	2.85e-2	3.53e-3

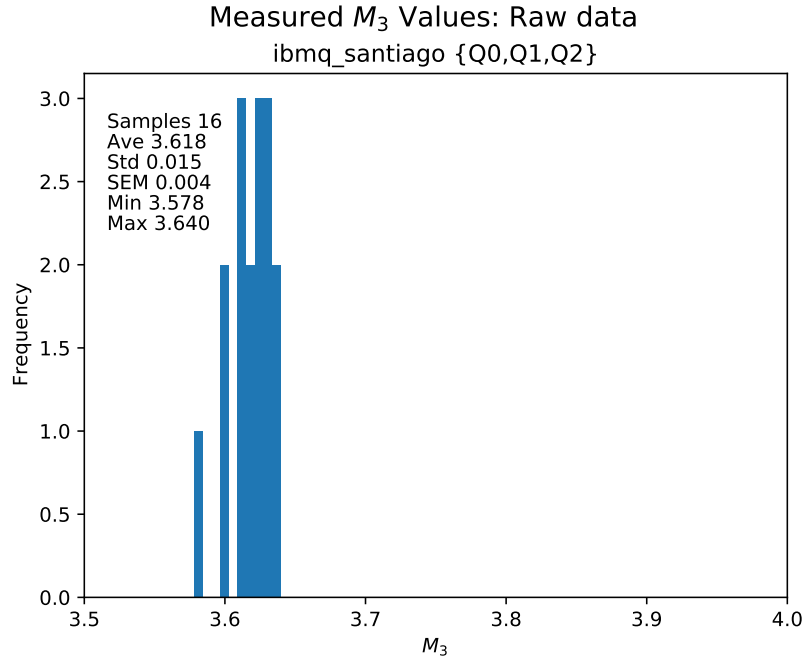


FIG. S3.

6. MERMIN POLYNOMIAL DATA

In this section the results of the $N=16$ independent measurements of the Mermin polynomials M_n , for $n=3$ and 4, are presented as histograms. For each M_n , the raw data values, the values corrected by a concurrently measured n -qubit T matrix, and the values corrected by the Γ matrix (using the L matrices from Table IV) are shown separately, but plotted on the same scale. Figures S3, S4, and S5 contain the M_3 results, and Figs. S6, S7, and S8 contain the M_4 results.

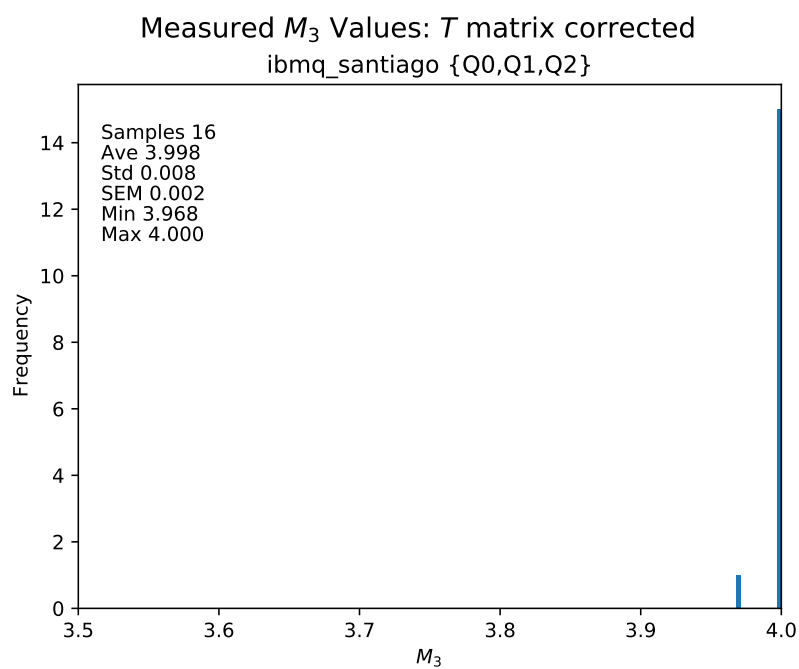


FIG. S4.

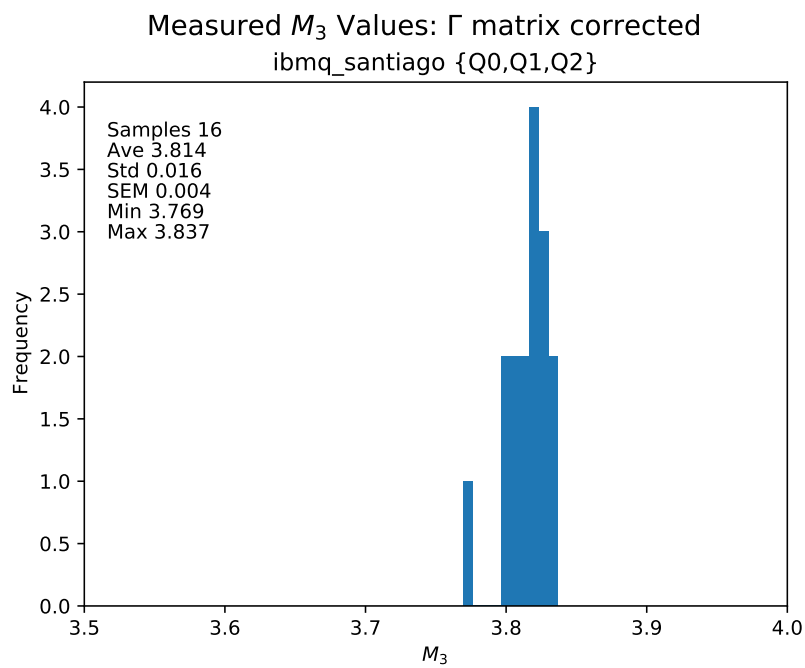


FIG. S5.

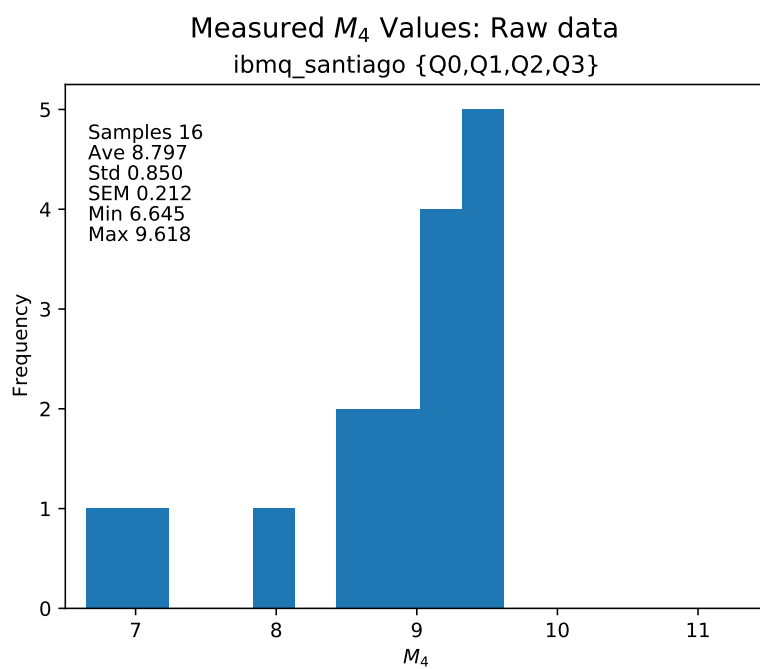


FIG. S6.

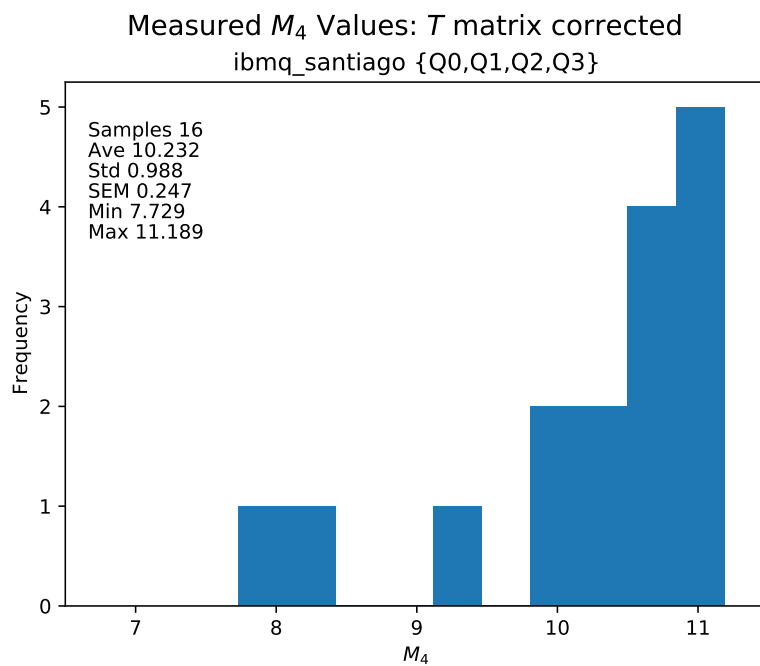


FIG. S7.

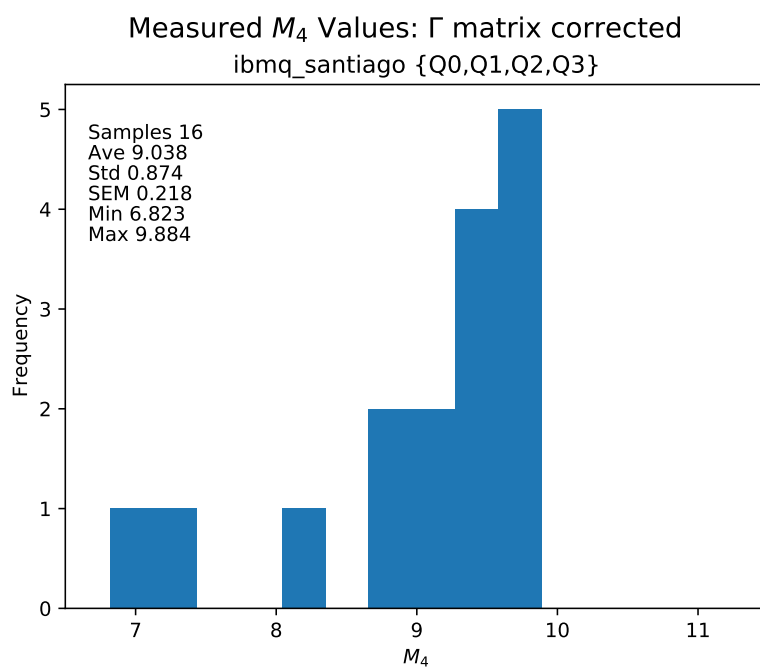


FIG. S8.

There is a long history of measuring Mermin polynomials on superconducting qubits. In Table VI we compare our measured values of M_3 and M_4 with results obtained previously.

TABLE VI. Comparison of Mermin polynomial measurements. Here n is the register size, LR is the maximum value consistent with local realism, and QM is the maximum value allowed by quantum mechanics. The last columns gives our error-mitigated results.

n	LR	QM	Neeley <i>et al.</i> [34]	DiCarlo <i>et al.</i> [36]	Alsina & Latorre [37]	Garcia <i>et al.</i> [38]	Gonzales <i>et al.</i> [39]	This work
3	2	4	2.08	3.40	2.85	2.84	3.34	3.81
4	4	$8\sqrt{2}$			4.81	5.42	9.07	9.04

7. SIMULATION

In this section we present the results of a complete end-to-end simulation of the conditionally rigorous TMEM technique applied the estimation of the 4-qubit Mermin polynomial

$$M_4 = \langle XXXY \rangle + \langle XXYX \rangle + \langle XYXX \rangle + \langle YXXX \rangle + \langle XXYX \rangle + \langle XYXY \rangle + \langle XYYX \rangle + \langle YXXY \rangle \\ + \langle YXYX \rangle + \langle YYXX \rangle - \langle XXXX \rangle - \langle YYYY \rangle - \langle YXYX \rangle - \langle YYYX \rangle - \langle YYYY \rangle \quad (S3)$$

on the depolarized GHZ state

$$\rho = (1 - \eta) |\psi\rangle\langle\psi| + \eta \frac{I}{d}, \quad (S4)$$

where $\eta \in [0, 1]$ is a noise parameter,

$$|\psi\rangle = \frac{|0000\rangle + e^{3\pi i/4}|1111\rangle}{\sqrt{2}}, \quad (S5)$$

and $d = 16$. We do this for all $0 \leq \eta \leq 1$. The simulation consists of the following steps:

- First construct a simplified but realistic error model for a noisy 4-qubit register, including imperfect $|0\rangle$ state preparation and $\pi/2$ rotations $G_{x,y}$, as well as a noisy multiqubit POVM. The fidelities of the $|0\rangle$ states and gates are chosen to approximately correspond to that measured on the ibmq_santago chip. The noisy 16-element POVM is diagonal but otherwise random, with the noise strength again consistent with ibmq_santago. Importantly, the POVM elements are *not* given as tensor products of single-qubit measurement operators. Call this the *exact error model* to contrast it with the approximate one predicted by GST in step B. Note that while the noisy states and gates are homogeneous across the register, the measurement errors are not.
- Perform single-qubit GST on each qubit in the register using synthetic input data generated by the exact error model, to approximately reconstruct the noisy $|0\rangle$ state and $\pi/2$ gates. Single-qubit measurement operators are also produced by GST but are not used here. Call this the *approximate error model* and denote it by ρ_0^{est} , $G_{x,y}^{\text{est}}$, and E_0^{est} for each qubit.
- Compute the L matrices from the GST output of step B.
- Use the exact error model from step A to simulate the experimental measurement of the Γ matrix. For comparison, also simulate the measurement of the T matrix. Call these the *synthetic* Γ and T matrices.
- Finally, assume that the noisy GHZ state (S4) has been prepared in the register, and simulate the measurement of the 4-qubit Mermin polynomial (19) in the presence of the noisy multiqubit POVM from step A. The depolarization in (S4) is intended to account for all errors incurred during the estimation of M_4 , including decoherence and imperfect tomography, but excluding multiqubit measurement errors (which are included separately in the noisy POVM). Therefore we can calculate both the noisy and exact measurement-error-free values of M_4 . Then perform TMEM on the Mermin polynomial with the synthetic Γ and T matrices, and compare with the exact values.

The simulation is repeated and averaged over $N = 16$ random POVM samples. Probabilities are assumed to be estimated with a large number of measurement samples and we do not include sampling errors in the simulation. Therefore, the only obstacle preventing perfect recovery of the measurement-error-free value of M_4 is the accuracy of the error model estimated by GST. In particular, if step B of the simulation is bypassed, and GST is rigged to return the exact error model of step A, exact values of the Mermin polynomial are always obtained.

Steps A-E are explained in detail for the interested reader in the following subsections. Here we briefly summarize the main result of the simulation, given in Table II. Here LR is the maximum value consistent with local realism. QM is the maximum value allowed by quantum mechanics. Simulated data are reported in the remaining columns: Exact($\eta = 0.2$) is the Mermin polynomial (19) calculated for the state (S4) with $\eta = 0.2$, chosen for consistency with the real experiment on ibmq_santago. Raw data is the same as Exact($\eta = 0.2$), but now calculated with the noisy multiqubit POVM from step A. The T and Γ columns give the polynomial values after correcting the synthetic probabilities with the synthetic T and Γ matrices. We observe that the average TMEM value based on Γ is close to the exact value (they become equal in the limit that GST works perfectly), validating the rigorous technique. However, we speculate that GST might need to choose its gauge differently on highly *unbalanced* error models, where one error source is much larger or smaller than the others.

TABLE VII. Simulated measurement and mitigation of the 4-qubit Mermin polynomial. Simulation results are reported as the average over $N = 16$ random POVM samples plus/minus the standard error σ/\sqrt{N} , where σ^2 is the variance of the N samples.

	LR	QM	Exact($\eta=0.2$)	Raw data	T matrix	Γ matrix
M_4	4	$8\sqrt{2}$	9.051	$8.962 \pm 1.8\text{e-}3$	$9.821 \pm 2.0\text{e-}5$	$9.067 \pm 9.2\text{e-}3$

A. Error model

First we build a simplified model for the noisy $|0\rangle$ states, $\pi/2$ rotations, and measurement operators consistent with those estimated by GST on the ibmq_santago chip. The model is simplified in that noise in $|0\rangle$ and the gates is modeled by depolarizing noise. The prepared $|0\rangle$ states on each qubit are given by

$$\rho_0 = \begin{pmatrix} 0.99 & 0 \\ 0 & 0.01 \end{pmatrix}, \quad (\text{S6})$$

which results from a 2e-2 depolarization error applied to the ideal $|0\rangle$ state. The state fidelity $F = \langle 0|\rho_0|0\rangle$ is 0.99, consistent with the experimental values reported by GST. In the Pauli basis this becomes

$$|\rho_0\rangle\rangle = \begin{pmatrix} 0.50 \\ 0 \\ 0 \\ 0.49 \end{pmatrix}, \quad (\text{S7})$$

where the components of any single-qubit state ρ are given by $|\rho\rangle\rangle_\sigma = \text{Tr}(\rho\sigma)/2$ for $\sigma \in \{I, X, Y, Z\}$.

The gates $G_{x,y}$ are similarly modeled as superoperators \mathcal{G}_μ corresponding to ideal $\pi/2$ rotations $e^{-i\pi X/4}$ and $e^{-i\pi Y/4}$ followed by a depolarization channel with 2e-4 depolarization error. In the Pauli basis these are 4×4 matrices with elements $(G_\mu)_{\sigma\sigma'} = \text{Tr}[\sigma \mathcal{G}_\mu(\sigma')]/2$, where $\mu = x, y$. In the exact error model they are given by

$$G_x = \begin{pmatrix} 1 & 0 & 0 & 0 \\ 0 & 0.9998 & 0 & 0 \\ 0 & 0 & 0 & -0.9998 \\ 0 & 0 & 0.9998 & 0 \end{pmatrix} \quad (\text{S8})$$

and

$$G_y = \begin{pmatrix} 1 & 0 & 0 & 0 \\ 0 & 0 & 0 & 0.9998 \\ 0 & 0 & 0.9998 & 0 \\ 0 & -0.9998 & 0 & 0 \end{pmatrix} \quad (\text{S9})$$

on each qubit. The gate fidelities $F = [\text{Tr}(G_{\mu,t}^\dagger G_\mu) + 2]/6$ with the unitary targets $G_{\mu,t}$ are 0.9999, consistent with the experimental values reported by GST.

The noisy POVM was generated iteratively by starting with the set of ideal projectors and randomly introducing small diagonal crosstalk errors in a way that guarantees that the 16 matrices remain positive semidefinite and that the set is properly normalized. The process is repeated until the noise level in the resulting Γ matrix (measured by the Frobenius distance from the identity, $\|\Gamma - I\|_F$) reaches the desired value. The synthetic POVM is not separable and contains correlated multiqubit measurement errors. The state ρ_0 , gates $G_{x,y}$, and POVM constitute the exact model error. The model does not include CNOT gates, which are not needed because the GHZ state preparation is described by the separate error model (S4).

B. GST

Next we use pyGSTi [58] to run GST on synthetic data generated by the exact error model (using the same hyperparameter settings as used in the real experiment). The output of GST is the *approximate error model*. As explained above, the approximate error model includes a *separable* estimate of the POVM (tensor products of the E_0^{est} and $E_1^{\text{est}} = I - E_0^{\text{est}}$), which we do not use. The approximate error model for the first of 16 random POVM instances is given in Table VIII. The measurement operators E_0^{est} differ from qubit to qubit because the noisy POVM from step A is not homogeneous across the qubits. While the gates are correctly recovered to high accuracy, there is a small variation in the reconstructed initial states ρ_0^{est} due to a small amount of measurement error bleeding into state preparation error.

TABLE VIII. Approximate error model estimated by GST using synthetic input data generated by the exact error model.

Qubit	ρ_0^{est}	G_x^{est}	G_y^{est}	E_0^{est}
1	$\begin{pmatrix} 0.9915 & 0 \\ 0 & 0.0085 \end{pmatrix}$	$\begin{pmatrix} 1 & 0 & 0 & 0 \\ 0 & 0.9998 & 0 & 0 \\ 0 & 0 & 0 & -0.9997 \\ 0 & 0 & 0.9998 & 0 \end{pmatrix}$	$\begin{pmatrix} 1 & -0 & 0 & 0 \\ 0 & 0 & 0 & 0.9997 \\ 0 & 0 & 0.9998 & 0 \\ 0 & -0.9998 & 0 & 0 \end{pmatrix}$	$\begin{pmatrix} 0.9937 & 0 \\ 0 & 0.0023 \end{pmatrix}$
2	$\begin{pmatrix} 0.9895 & 0 \\ 0 & 0.0105 \end{pmatrix}$	$\begin{pmatrix} 1 & 0 & 0 & 0 \\ 0 & 0.9998 & 0 & 0 \\ 0 & 0 & 0 & -0.9997 \\ 0 & 0 & 0.9998 & -0 \end{pmatrix}$	$\begin{pmatrix} 1 & 0 & 0 & 0 \\ 0 & 0 & 0 & 0.9997 \\ 0 & 0 & 0.9998 & 0 \\ 0 & -0.9998 & 0 & -0 \end{pmatrix}$	$\begin{pmatrix} 0.9937 & 0 \\ 0 & 0.0042 \end{pmatrix}$
3	$\begin{pmatrix} 0.9873 & 0 \\ 0 & 0.0127 \end{pmatrix}$	$\begin{pmatrix} 1 & 0 & 0 & 0 \\ 0 & 0.9998 & 0 & 0 \\ 0 & 0 & 0 & -0.9997 \\ 0 & 0 & 0.9998 & 0 \end{pmatrix}$	$\begin{pmatrix} 1 & 0 & 0 & 0 \\ 0 & 0 & 0 & 0.9997 \\ 0 & 0 & 0.9998 & 0 \\ 0 & -0.9998 & 0 & 0 \end{pmatrix}$	$\begin{pmatrix} 0.9958 & 0 \\ 0 & 0.0085 \end{pmatrix}$
4	$\begin{pmatrix} 0.9906 & 0 \\ 0 & 0.0094 \end{pmatrix}$	$\begin{pmatrix} 1 & 0 & 0 & 0 \\ 0 & 0.9998 & 0 & 0 \\ 0 & 0 & 0 & -0.9997 \\ 0 & 0 & 0.9998 & 0 \end{pmatrix}$	$\begin{pmatrix} 1 & 0 & 0 & 0 \\ 0 & 0 & 0 & 0.9997 \\ 0 & 0 & 0.9998 & 0 \\ 0 & -0.9998 & 0 & 0 \end{pmatrix}$	$\begin{pmatrix} 0.9958 & 0 \\ 0 & 0.0053 \end{pmatrix}$

C. L matrices

The L matrix calculated from the exact error model (the same on every qubit) is

$$L = \begin{pmatrix} 0.9900 & 0.0100 & 0 & 0 \\ 0.0102 & 0.9898 & 0 & 0 \\ 0.0101 & 0.0101 & 0.9798 & 0 \\ 0.0103 & 0.0103 & 0 & 0.9794 \end{pmatrix}. \quad (\text{S10})$$

The L matrices calculated from synthetic GST data are all close to (S10) and are given in Table IX for the first of 16 random POVM instances.

TABLE IX. L matrices calculated from the approximate error model produced by GST.

Qubit	L
1	$\begin{pmatrix} 0.9915 & 0.0085 & 0 & 0 \\ 0.0087 & 0.9913 & 0 & 0 \\ 0.0086 & 0.0087 & 0.9827 & 0 \\ 0.0089 & 0.0089 & 0 & 0.9823 \end{pmatrix}$
2	$\begin{pmatrix} 0.9895 & 0.0105 & 0 & 0 \\ 0.0108 & 0.9893 & 0 & 0 \\ 0.0106 & 0.0107 & 0.9787 & 0 \\ 0.0109 & 0.0109 & 0 & 0.9782 \end{pmatrix}$
3	$\begin{pmatrix} 0.9874 & 0.0127 & 0 & 0 \\ 0.0129 & 0.9871 & 0 & 0 \\ 0.0128 & 0.0128 & 0.9744 & 0 \\ 0.0131 & 0.0131 & 0 & 0.9739 \end{pmatrix}$
4	$\begin{pmatrix} 0.9906 & 0.0095 & 0 & 0 \\ 0.0097 & 0.9903 & 0 & 0 \\ 0.0096 & 0.0096 & 0.9808 & 0 \\ 0.0099 & 0.0098 & 0 & 0.9803 \end{pmatrix}$

D. Γ and T matrices

The synthetic Γ matrix is calculated from

$$\Gamma(x|x') = \sum_{\lambda_1 \cdots \lambda_n} (L_1^{-1})_{x'_1 \lambda_1} \cdots (L_n^{-1})_{x'_n \lambda_n} \text{tr}(E_x \rho_{\lambda_1} \cdots \rho_{\lambda_n}), \quad (\text{S11})$$

using the L matrices from Table IX. The *exact* error model is used to calculate $\text{tr}(E_x \rho_{\lambda_1} \cdots \rho_{\lambda_n})$. The synthetic T matrix is calculated from

$$T(x|x') = \text{tr}(E_x \rho_{x'}), \quad (\text{S12})$$

where E_x and $\rho_{x'}$ are obtained from the exact error model.

E. Mermin polynomial

Finally, we simulate the measurement of the Mermin polynomial (19) in the presence of the noisy multiqubit POVM from step A. We assume that the noisy GHZ state (S4) has been prepared in the register and we calculate both the noisy and measurement-error-free values of M_4 . Then we perform TMEM with the synthetic Γ and T matrices, and compare with the exact values. We do this as a function of GHZ state depolarization error η , with the results of the first of 16 random POVM instances summarized in Figs. S9 and S10.

Figure S9 contains four curves. The solid red curve is the exact value of M_4 in the state (S4) with no measurement error. The dotted purple curve is the raw data value of M_4 that would be measured in the presence of the noisy POVM from the exact error model. It is obtained by including the noisy POVM in each expectation value measurement in (19). The dashed purple curve is the result of applying TMEM with the synthetic T matrix. It overestimates M_4 because the T matrix is corrupted by the presence of imperfect state preparation. The solid purple curve (obscured by the solid red line) is the result of applying TMEM with the synthetic Γ matrix. The results in Table II agree with the $\eta = 0.2$ case in Fig. S9. The differences between the exact and Γ -corrected values are too small to be seen in Fig. S9, but are directly plotted in Fig. S10 on a logarithmic scale.

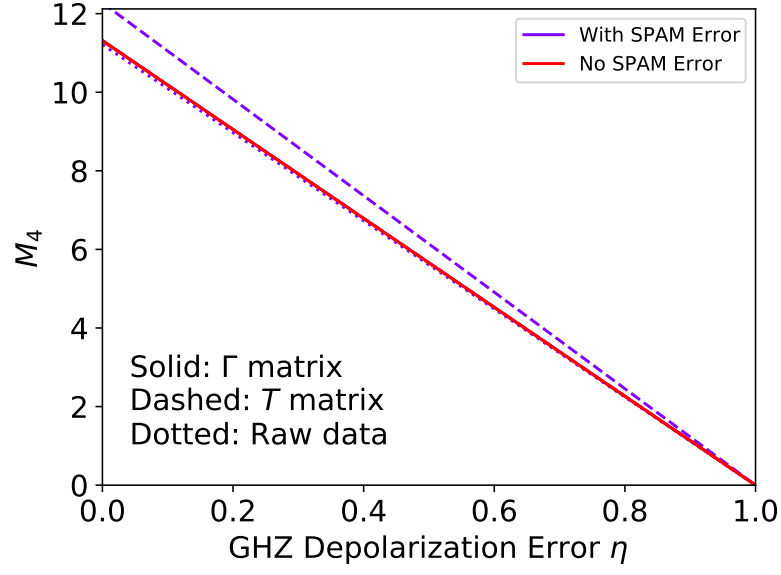


FIG. S9. Result of TMEM applied to noisy Mermin polynomial measurement.

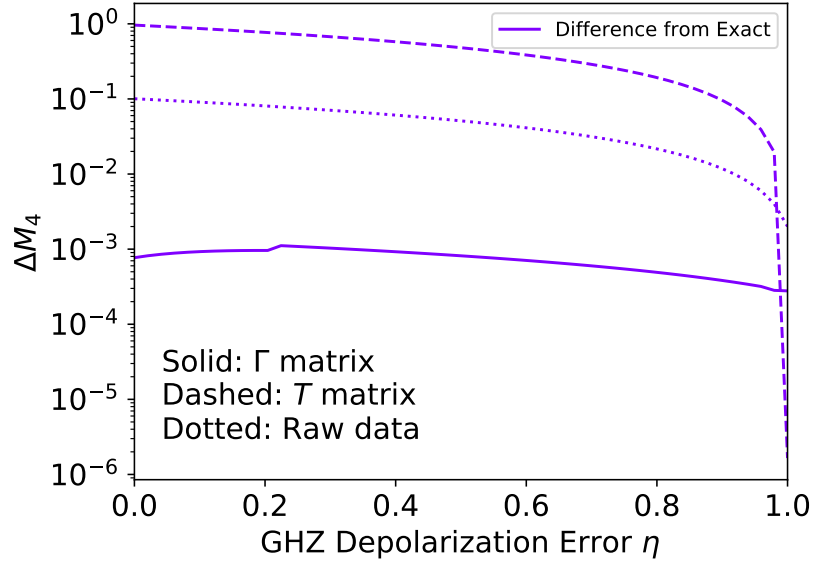


FIG. S10. Data from Fig. S9 replotted as magnitudes of differences of raw and corrected values from the exact measurement-error-free value.